Strain partitioning and factorization in a quartz arenite

CHARLES M. ONASCH and BINGMING SHEN-TU*

Department of Geology, Bowling Green State University, Bowling Green, OH 43403, U.S.A.
E-mail: conasch@bgnet.bgsu.ed

and

BRENT A. COUZENS-SCHULTZ†

The Center for Tectonophysics, Department of Geology and Geophysics, Texas A&M University,
College Station, TX 77843, U.S.A.

Abstract—Most rocks deform by multiple grain-scale deformation mechanisms. In order to assess completely the contributions of each mechanism, the strain associated with that mechanism must be known and compared to the finite strain. This study describes the partitioning of strain between three mechanisms, pressure solution, dislocation creep, and microfracturing, in a quartz arenite deformed at low temperatures. Pressure solution, which occurred primarily during compaction, dominates the finite strain with an average of 24% shortening normal to bedding. Dislocation creep, which occurred during layer-parallel shortening, accounts for about 2% shortening parallel to bedding dip. Microfractures, which occur in three orthogonal sets, resulted in 2–4% extension normal to bedding, parallel to bedding strike, and parallel to bedding dip. The validity of the mechanism strains was tested using strain factorization. Models were constructed using the mechanism strains in an order determined by their relative ages. Because porous, well-sorted quartz arenites, such as the one studied, are likely to undergo some mechanical compaction in the early stages of diagenesis, variable amounts of mechanical compaction were included in factorization models. Models using the measured deformation mechanism strains with an initial 5–10% mechanical compaction yield finite strains in close agreement with the measured finite strains. This suggests that the mechanisms identified, the strain associated with each mechanism, and the deformation sequence are plausible. © 1998 Elsevier Science Ltd. All rights reserved

INTRODUCTION

Deformation of rocks occurs by more than one grain-scale mechanism, operating either concurrently or sequentially. Understanding how the deformation is partitioned between different mechanisms is basic to understanding the deformation process. Although recognizing the operative mechanisms by their characteristic microstructures is straightforward, determining the contribution of each has proven difficult owing to the scarcity of strain methods specific to individual deformation mechanisms.

Partitioning of the deformation into individual deformation mechanisms can be done qualitatively or quantitatively. Point-counting key microstructures can give a general idea about the relative importance of associated deformation mechanisms (Onasch and Dunne, 1993), but can be misleading (Onasch, 1993; Harrison, 1997). For example, undulatory extinction is nearly ubiquitous in weakly deformed rocks (Tullis *et al.*, 1973; Hirth and Tullis, 1992). Point-counting would lead to an overestimate of the importance of dislo-

cation creep. Quantitative assessment requires that the strain associated with each mechanism, along with the finite strain, be measured. With a few notable exceptions (e.g. Mitra, 1976; Wu and Groshong, 1991), this has proven to be a difficult task.

The final step in a complete understanding of the deformation is to determine the strain history. By integrating a sequence of deformational events with the mechanism strains associated with each event, the strain history can be determined. The proposed history can be validated by comparing factorized finite strains, determined from the mechanism strains, to the measured finite strains. Any discrepancy between the factorized strains and the finite strain can indicate errors in one or more strain determinations, an incorrect strain history, or an unrecognized deformation mechanism.

The purpose of this paper is to illustrate how the complete strain history of a rock can be determined through identification of the operative deformation mechanisms, determination of strains associated with each mechanism, and integration of the mechanism strains into a deformation sequence determined by microstructure cross-cutting relations. The results of this approach are then compared to the finite strain using strain factorization. The lithology used is a quartz arenite deformed at low temperatures and

---

*Present address: Department of Earth and Space Sciences, SUNY at Stony Brook, Stony Brook, NY 11794, U.S.A.
†Shell E&P Technology Co., P.O. Box 481, Houston, TX 77001, U.S.A.

pressures; however, the methods used are general enough to be applicable to a wide range of lithologies and settings.

Geologic setting

The 13 samples used in this study are from the Lower Silurian Massanutten Sandstone. The sandstone consists of about 200 m of medium-grained, framework-supported, quartz arenite interbedded with quartz pebble conglomerates. The unit is exposed in an overturned synclinorium located along the axis of the Great Valley province in the central Appalachian foreland (Fig. 1). The synclinorium is rootless and part of the Blue Ridge thrust sheet, which together with the underlying North Mountain thrust sheet, was transported northwestward some 65 km during the Late Paleozoic Alleghanian orogeny (Evans, 1989). Deformation took place at 5–6 km depth and 150–250°C (Epstein et al., 1977; Harris, 1970).

The samples are from a variety of structural settings including upright and overturned limbs, and fold hinges. On the basis of texture, microstructures present, microstructural history, and strain, they are believed to be representative of the more than 200 samples that have been examined in this area (Onasch, 1984, 1990).
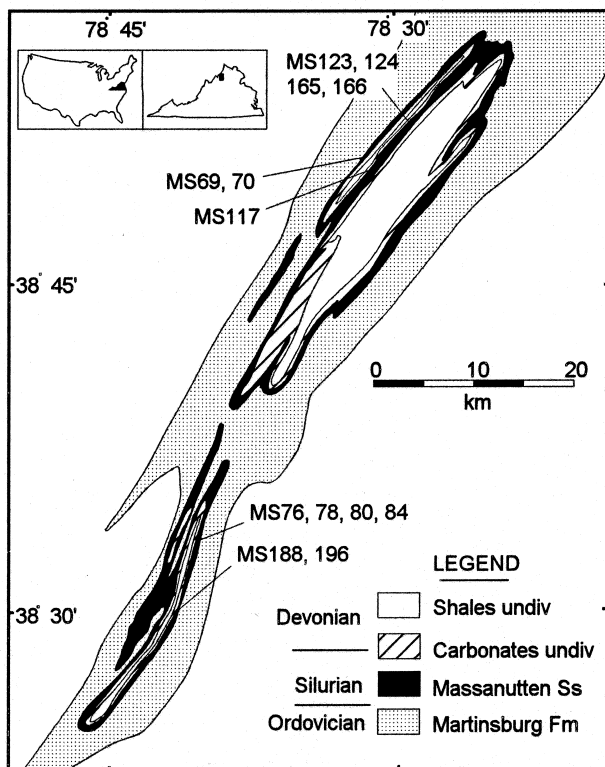

Fig. 1. Generalized geologic map of the Massanutten synclinorium showing location of Massanutten Sandstone samples used in the study.

Microstructures

Transmitted and cathodoluminescence light petrography reveal that grain-scale deformation of the quartz arenite occurred by pressure solution, dislocation creep, and microfracturing. Pressure solution microstructures include sutured and interpenetrating grains (Fig. 2a). Where clay matrix is present, accumulations of clay lie along dissolution surfaces as stylolites. The dissolution surfaces are irregular, but tend to parallel bedding. Microstructures indicative of dislocation creep include, in order of decreasing abundance, undulatory extinction, deformation lamellae (Fig. 2b), and deformation bands (Fig. 2c). A few occurrences of subgrains and grain boundary migration recrystallization were seen in high strain (fault) zones, but are not considered significant. Brittle microstructures include fluid inclusion planes (Fig. 2d) and microveins (Fig. 2e). The lack of offset indicates that both are healed Mode I microfractures. Fluid inclusion planes are less than 10 μm wide whereas microveins range from 10 to 100 m in width (Onasch, 1990). Microveins parallel fluid inclusion planes and both occur in three orthogonal sets with remarkably consistent orientations relative to bedding and local strike. They are bedding-parallel, bedding-normal/strike-parallel, and bedding-normal/dip-parallel (Onasch, 1990).

Cross-cutting relations between microstructures establish the relative ages of deformation mechanisms. Bedding-parallel stylolites and pressure solution features are the oldest microstructures as they commonly are truncated by diagenetic pore-filling cement. Dislocation creep microstructures are next oldest. Deformation lamellae, deformation bands, and subgrains are found in both detrital grains and cement; hence post-date the pressure solution features. Fluid inclusion planes cross deformation lamellae (Fig. 3a) and deformation bands (Fig. 3b) undeflected, indicating microfractures are the youngest microstructures. A small amount of pressure solution post-dating microfracturing is shown by rare instances of microveins being offset along dissolution surfaces oriented at a high angle to bedding. Although some microstructures might be inherited from the source rocks of the Massanutten Sandstone, most can be shown to have formed in-situ. For example, deformation lamellae extend from detrital grains into the optically continuous overgrowth cement (Fig. 3c) as do fluid inclusion planes (Fig. 3d) and microveins (Fig. 2e). Restriction of recrystallization to fault zones also argues for formation in-situ.

METHODS

Strains were determined from three, mutually-perpendicular thin sections from each of the 13 samples
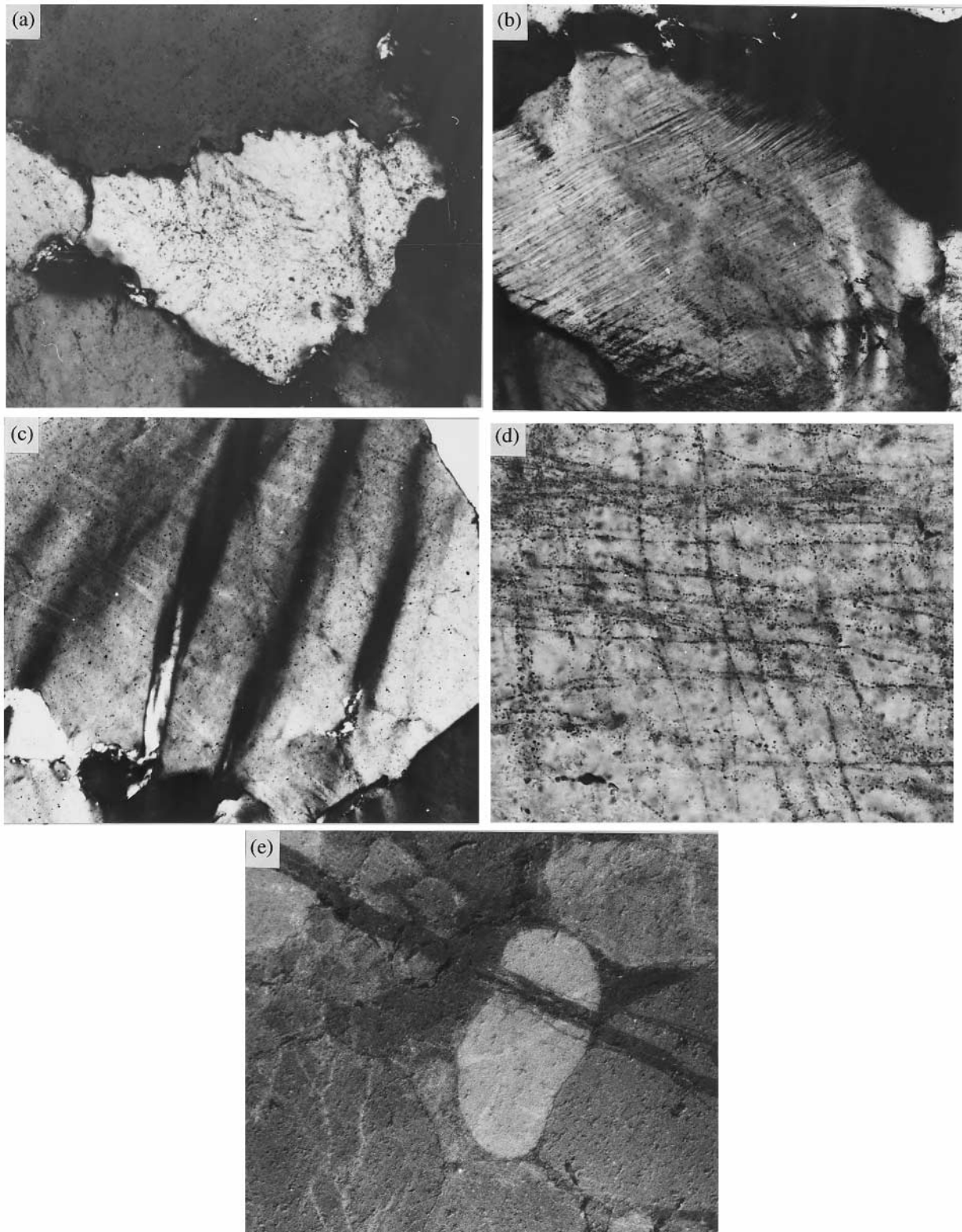
Fig. 2. Photomicrographs of microstructures in the Massanutten Sandstone. (a) Sutured and interpenetrated grain boundaries; (b) deformation lamellae; (c) deformation bands; (d) two sets of orthogonal fluid inclusion planes; (e) microvein. Width of all photomicrographs is 1.8 mm except (d) which is 0.3 mm. All are in crossed polarized light except (e) which is in cathodoluminescence.

used in this study. Using bedding as a reference direction, thin sections were cut parallel to bedding; bedding-normal, strike-parallel; and bedding-normal, dip-parallel. For the finite strain and strain associated with each deformation mechanism, the geometry of the strain ellipsoid was calculated from strain ellipses
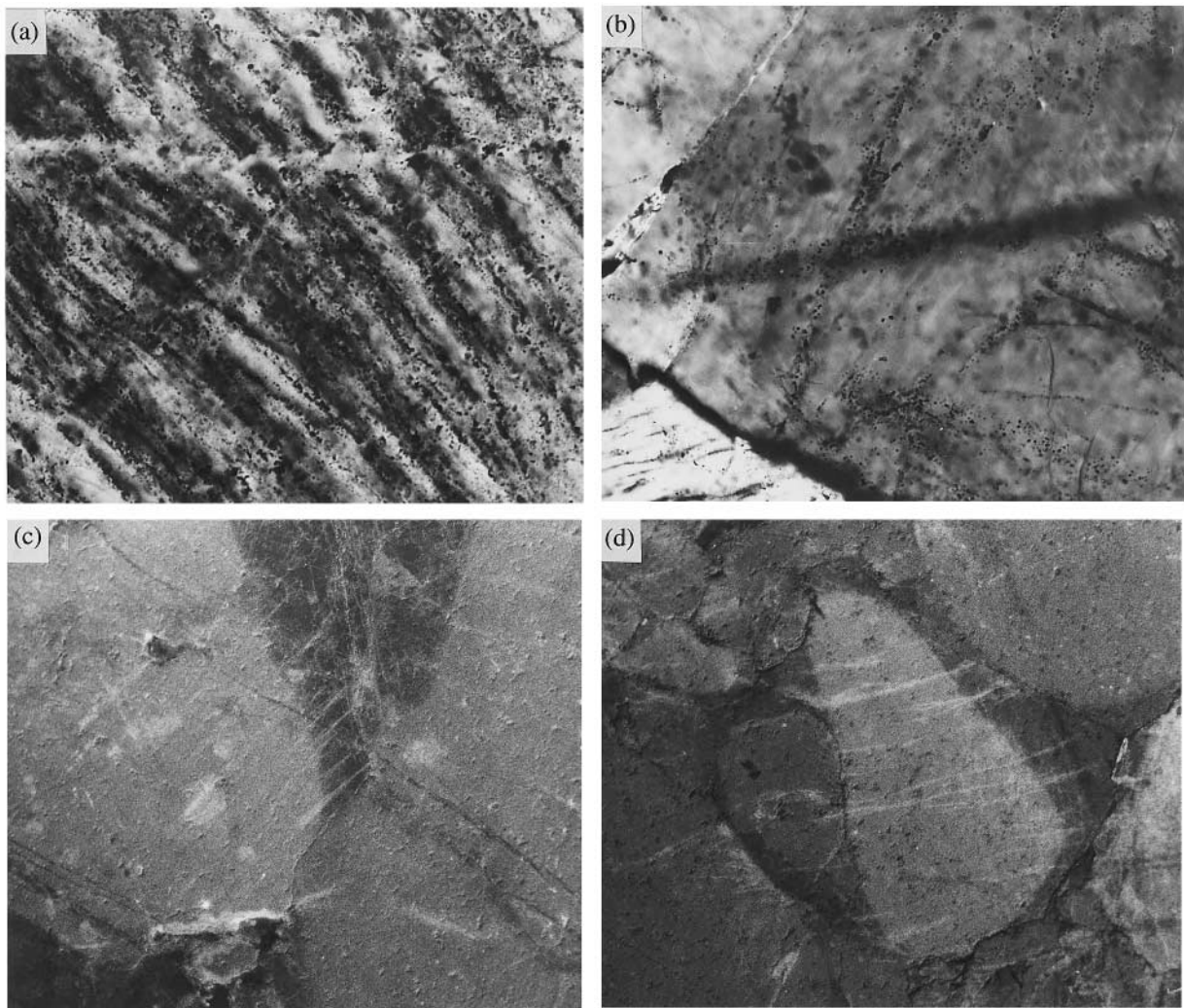
Fig. 3. Relative age relations between microstructures. (a) Fluid inclusion plane (horizontal) cutting deformation lamellae; (b) fluid inclusion plane (near vertical) crossing deformation band (subhorizontal) undeflected; (c) deformation lamellae extending from detrital grain into optically continuous overgrowth cement (dark); (d) fluid inclusion planes (bright lines) extending across several detrital grains and into overgrowth cement. Width of photomicrographs (a) & (b) are 0.3 mm; (c) & (d) are 1.8 mm. (a) & (b) are in crossed polarized light; (c) & (d) are in cathodoluminescence.

determined for the three perpendicular sections using the method of Owens (1984).

Finite strain

The finite strain was determined using a normalized version of the Fry method (Erslev, 1988). Grain outlines were digitized from cathodoluminescence photomicrographs so that detrital grain outlines could be differentiated from overgrowth cement. Failure to use the original detrital grain outlines can lead to errors, especially in low strain rocks (Dunne *et al.*, 1991). In order to get sufficient point density to determine confidently the strain ellipse, at least 300 grains were digitized in each section.

Pressure solution strain

Pressure solution strain was measured using the pressure solution strain (PSS) method (Onasch, 1993).

The PSS method measures only shortening and does not take into account extension associated with overgrowths or pressure shadows. In our case, the samples studied lacked overgrowths or pressure shadows. Therefore, the PSS method gives a full account of pressure solution strain.

The amount and direction of shortening is measured by the PSS method using the geometry of truncated and interpenetrated grains. For any two pressure-solved grains (e.g. Fig. 2a), the shortening normal to the compromise boundary can be found by measuring the present distance between the grain centers and the original distance determined by reconstructing the grain outlines. The results can be represented by a point plotted relative to a circle such that the distance in from the edge of the circle is proportional to the shortening and the azimuth is parallel to the shortening direction. When done for a number of grain pairs (>50), a Fry-like plot is produced to which an ellipse is fitted to the central void giving the geometry of the

pressure solution strain. A complete description of the method, along with an evaluation of its applicability, is found in Onasch (1993).

Dislocation creep strain

The strain due to dislocation creep was determined from deformation bands using the quartz strain gage (Wu and Groshong, 1991). Deformation bands (Fig. 2c) are narrow zones where the crystal lattice has been rotated relative to the surrounding portions of the grain (Carter, 1968). Laboratory deformation of quartz aggregates and single crystals indicates that the deformation bands are subparallel to the c-axis with maximum resolved shear strain on [0001] parallel to an a-axis (Carter et al., 1964; Christie et al., 1964). The quartz strain gage uses the geometry of deformation bands to calculate the shear strain for each grain. The strain of the aggregate is found by simultaneous solution of the strains from at least five grains (Wu and Groshong, 1991). In this study, at least 25 grains were used from each mutually-perpendicular thin section.

Microfracture strain

Because all microfractures are Mode I fractures, extensional strain can be determined using the width of the microfracture and microfracture spacing (Onasch, 1990, 1994). For fluid inclusion planes, the inclusion diameter and inclusion spacing along an inclusion plane were used to calculate the total area of the inclusions along that plane. Assuming that the area of the inclusions is equal to the area of the original microfracture, the width of the original microfracture can be determined. From the widths and the spacing of inclusion planes, the extensional strain normal to the inclusion planes can be calculated. This method may underestimate the extensional strain if the initial open space in the microfracture was not totally captured as fluid inclusions (e.g. see fig. 2e of Lloyd and Knipe, 1992). For microveins, extensional strains were measured from the total width along a traverse normal to the microveins. Measurement of microvein widths was done in cathodoluminescence because the vein quartz is in optical continuity with wall rock grains and is indistinguishable in transmitted light. Where there was more than one set of microfractures, three dimensional strains were computed from the extensions of individual sets, a task made easier by the orthogonal relationship between sets.

Strain factorization

In order to do strain factorization we assume that the strain for each measured mechanism is related to one event, and we use the cross-cutting relations of the microstructures to determine the sequence of events. First, for each mechanism, a deformation matrix, **M**, is determined from the measured principal axis orientations and extensions. **M** is determined in a coordinate system coincident with the measured strain ellipsoid axes, where $+x$, $+y$, and $+z$ parallel the long, intermediate, and short axes in their respective plunge directions. As a result, all off-axis terms in the matrix, **M**, are zero and the terms along the diagonal are determined by adding the extension along each axis to one. Using direction cosine matrices, **M** is transformed to a coordinate system used for all the samples that has x, y, and z parallel to strike of bedding, dip direction of bedding, and normal to bedding, respectively. The new matrix, **D**, is a deformation matrix that maps points from an undeformed to a deformed state in our standard coordinate system. **D** represents the deformation accommodated by one mechanism. As a check, a matrix, **E**, representing the resultant strain ellipsoid due to the deformation **D** can be calculated simply by $\mathbf{E} = \mathbf{D}^{-1}\mathbf{D}_t^{-1}$ (Couzens et al., 1993), and this can be compared to the input ellipsoid to ensure the correct **D** was calculated. For each sample, a deformation matrix was calculated for the pressure solution strain, $\mathbf{D}_{psol}$, the dislocation creep strain, $\mathbf{D}_{disl}$, and the microfracture strain, $\mathbf{D}_{frac}$. These matrices may then be multiplied together to determine a resultant finite strain that can be compared to the measured finite strain.

To do the factorization, the temporal sequence of deformation mechanism must be known because matrix multiplication, and hence factorization, is not commutative. Based on microstructural relations described above, the sequence used, from oldest to youngest, was: (1) pressure solution, (2) dislocation creep, and (3) microfracturing. In addition to the described mechanisms' strains, mechanical compaction was included in the sequence before pressure solution because it probably contributes to the finite strain. Well-sorted sandstones such as the Massanutten typically undergo about 10% mechanical compaction before chemical compaction (pressure solution) starts (Manus and Coogan, 1974; Houseknecht, 1988). Mechanical compaction is accommodated by grain boundary sliding which leaves no microstructural signature and therefore could not be quantified in this study as a separate mechanism. Although compaction was recorded by the finite strain analysis, it cannot be assigned to one of the deformation mechanisms investigated. Therefore, to account for this compaction, a deformation matrix, $\mathbf{D}_{comp}$, was included in each factorization and was varied in 5% increments from 0% to 20% uniaxial shortening normal to bedding. Five finite deformations, one for each value of mechanical compaction, were calculated for each sample as, $\mathbf{D}_{finite} = \mathbf{D}_{frac}\,\mathbf{D}_{disl}\,\mathbf{D}_{psol}\,\mathbf{D}_{comp}$, where the oldest event is on the right. From these, finite strain ellipsoids were calculated, as shown above, and compared to the measured finite strain for that sample.

RESULTS

Finite strain

Histograms of the finite strain ratios for the three principal planes are shown in Fig. 4. Finite strains are generally low, typical of quartz arenites in the Appalachian foreland (Onasch and Dunne, 1993; Couzens, 1993; Thorbjornsen and Dunne, 1997). Mean finite strain ratios in the *XY*, *YZ*, and *XZ* principal planes are 1.17, 1.20, and 1.40, respectively. On a Flinn diagram, the strains show no preference for either the flattening or constrictional field (Fig. 5a).

The geometry of the three principal axes is shown in Fig. 6. There is a consistent relationship between the strain geometry and bedding regardless of the present bedding orientation or structural position. *X*-axes are parallel to bedding strike, *Y*-axes are parallel to bedding dip, and *Z*-axes are normal to bedding.

Mechanism strains

Pressure solution strain magnitudes are similar to the finite strains (Figs 4 & 5b) with mean *XY*, *YZ*, and *XZ* strain ratios of 1.14, 1.15, and 1.30, respectively. The mean extensions are $e_x = 0\%$, $e_y = -11\%$, and $e_z = -24\%$. The principal axes also show the same consistent relationship to bedding as did the finite strain axes, except the degree of preferred orientation is not as strong for the *X* and *Y*-axes (Fig. 6).
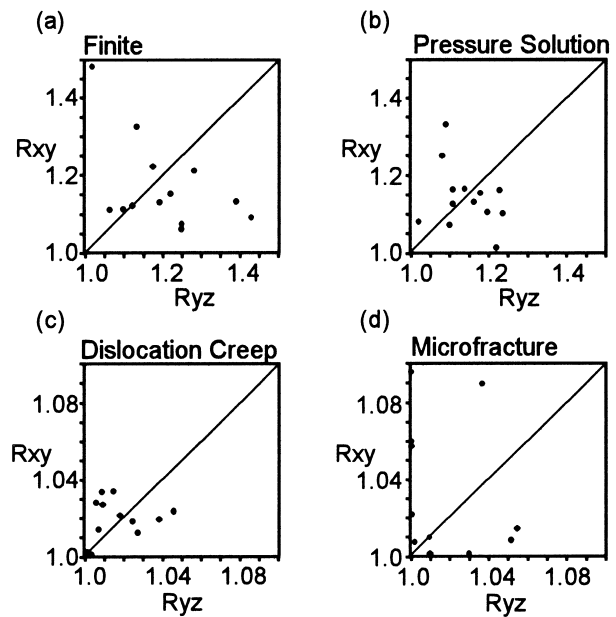
Fig. 5. Flinn diagrams of (a) finite; (b) pressure solution; (c) dislocation creep; and (d) microfracture strains. $N = 13$ for each diagram.

Compared to the finite and pressure solution strains, dislocation creep strains are low, with mean *XY*, *YZ*, and *XZ* ratios of 1.02, 1.03, and 1.04, respectively (Fig. 4). Like the other strains, there is no preference for either the flattening or constrictional fields on a Flinn plot (Fig. 5c). The mean extensions are $e_x = 2.1\%$, $e_y = 0.2\%$, and $e_z = -2.2\%$. Despite the low strain magnitudes, there is a strong preferred orientation to each of the principal axes that is well above the level of statistical significance (3σ contour on a Kamb-contoured stereoplot). The *X*- and *Y*-axes define a girdle normal to bedding and parallel to strike, with *X*-axes concentrated normal to bedding and *Y*-axes parallel to the strike of bedding (Fig. 6). *Z*-axes define a strong maxima parallel to the dip of bedding.

Like the dislocation creep strains, microfracture strains are low, with mean *XY*, *YZ*, and *XZ* ratios of 1.03, 1.02, and 1.04, respectively (Fig. 4). The mean extensions are $e_x = 4.4\%$, $e_y = 2.0\%$, and $e_z = 1.6\%$. On a Flinn diagram, samples with one microfracture set plot on one of the axes. Samples with two sets plot on or off the axes depending on the relative magnitude of the extensional strains, and samples with three sets plot off either axis in the constrictional or flattening fields (Fig. 4d). The principal axes are also related to bedding, as would be expected by the relationship of the microfracture sets to bedding described earlier. *X*- and *Y*-axes are parallel to bedding and *Z*-axes are normal to bedding (Fig. 6).

Strain factorization

Factorization using the mechanism strains yields results very similar to the measured finite strains both in magnitude and orientation (Table 1, Figs 7 & 8).
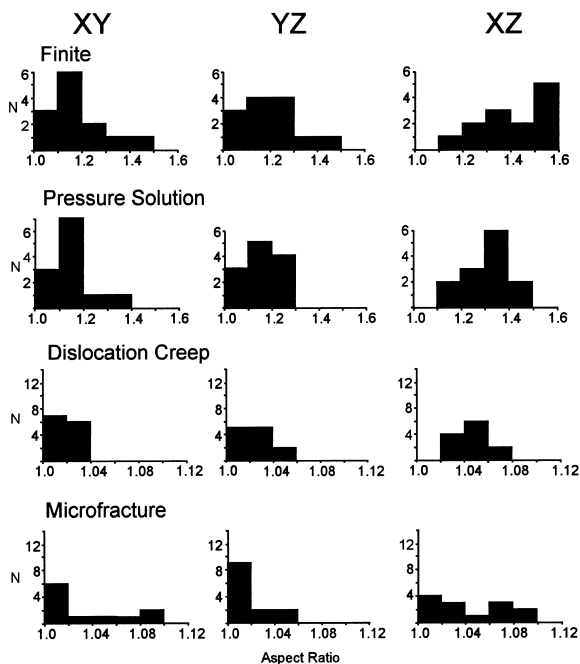

Fig. 4. Frequency histograms of strain magnitude data for finite, pressure solution, dislocation creep, and microfracture strains. $N = 13$ for each plot. Note that horizontal scales are different for dislocation creep and microfracture strains than for finite and pressure solution strains.
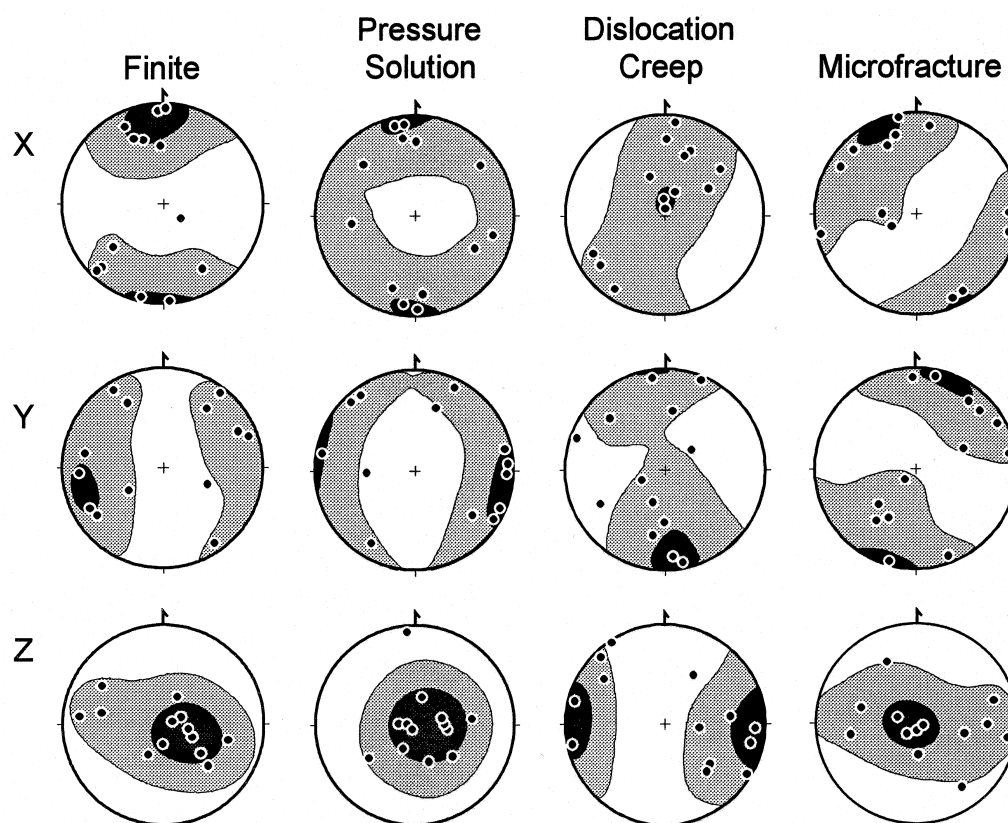
Fig. 6. Principal axis orientations for finite, pressure solution, dislocation creep, and microfracture strains. $N = 13$ for each plot. Contours are at 3 and 6σ. All data have been rotated with bedding so that bedding is horizontal and strike is north.

The factorization procedure neither consistently over- nor underestimates the measured finite strains. On average, the best results were obtained with a mechanical compaction of from 5 to 10%, although factorization models with 0–12% fall within one standard deviation of the average measured finite strain (Fig. 8). The measured finite strains for most samples fall on or very near a trend of finite strains predicted by the factorizations with variable mechanical compaction (Fig. 8). Although the average mechanical compaction

for all the samples is between 5 and 10%, the factorization of individual samples shows mechanical compaction values ranging from 0 to 25 + % (e.g. MS76 and MS165, Fig. 8). The large mechanical compaction needed for MS165 may be explained by the relatively small amount of bed-normal shortening (9%) recorded by the pressure solution strain in that sample. In general, the mechanical compaction and the bed-normal component of the pressure solution strain, which records chemical compaction, add up to 25–35% total

Table 1. Difference between finite and factorized strain ratios for no compaction and 10% compaction cases. Differences are (finite strain − factorized strain). Means are calculated using the absolute value of the ratio difference

| Sample	No compaction			10% compaction		
	R_{xy}	R_{yz}	R_{xz}	R_{xy}	R_{yz}	R_{xz}
MS69	0.20	−0.04	0.18	0.21	−0.15	0.08
MS70	0.03	−0.07	−0.05	0.03	−0.20	−0.18
MS76	0.03	−0.01	0.03	0.03	−0.14	−0.13
MS78	−0.09	0.15	0.06	−0.05	0.10	0.05
MS80	0.00	0.14	0.16	0.01	0.03	0.04
MS84	−0.02	0.20	0.22	−0.02	0.08	0.07
MS117	0.08	0.08	0.18	0.08	−0.04	0.05
MS123	0.06	−0.08	−0.02	−0.03	−0.03	−0.06
MS124	−0.07	0.00	−0.07	−0.07	0.00	−0.07
MS165	−0.03	0.37	0.37	−0.03	0.26	0.24
MS166	−0.24	0.17	−0.08	−0.25	0.10	−0.18
MS188	0.12	−0.10	−0.02	−0.02	0.00	−0.02
MS196	0.04	−0.17	−0.14	0.04	−0.28	−0.26
Mean	0.08	0.12	0.12	0.07	0.11	0.11

Factorized Strains
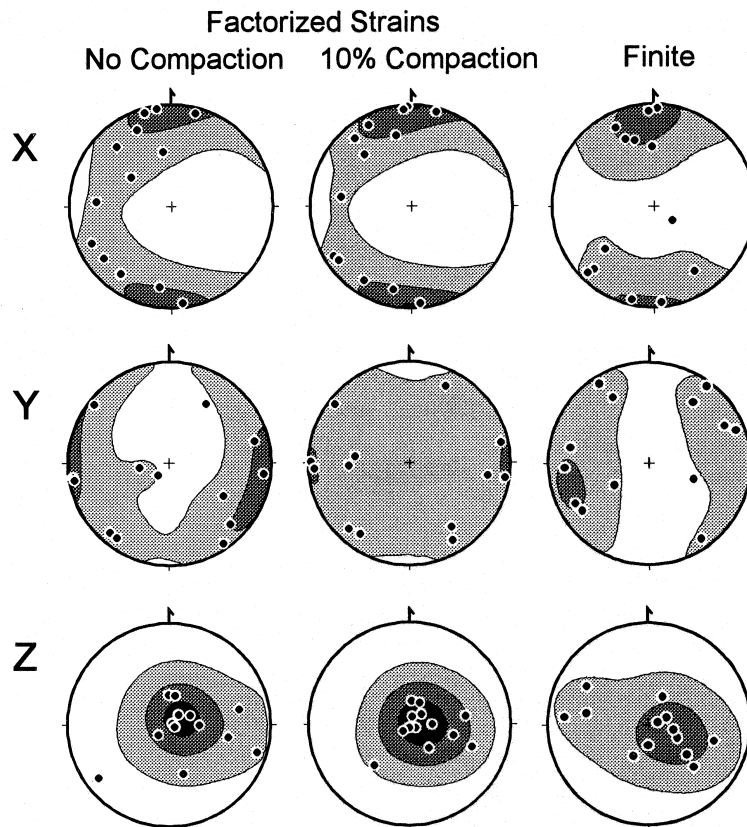
Fig. 7. Comparison of factorized and finite principal strain axis orientations. $N = 13$ for each plot. Contours for factorized and finite strain axes are at 3, 6 and 9σ. All data have been rotated so that bedding is horizontal and strike is north.

compaction. This is in agreement with studies of compaction in sandstones that have grain-to-grain truncations and minimal porosity (Houseknecht, 1988) as well as previously inferred compactions for the laterally equivalent Tuscarora Sandstone (Couzens et al., 1993).

Two samples (MS70 and MS196) fall on the factorization model trend, but are best fit by a negative mechanical compaction. Possible explanations for this include an overestimate of the pressure solution strain or an underestimate of strain related to bed-parallel microfractures. Two samples (MS69 and MS166) fall significantly off the trend of the factorization models, suggesting a missed strain event or incorrectly measured strain.

For most individual cases, and for the sample population as a whole, the ratios of measured finite strains fall on the trend of factorized strain models (Fig. 8). In all cases, the orientation of measured finite strain ellipsoid axes corresponds to factorized strain ellipsoid axes (Fig. 8). The good agreement between factorized and measured strains suggests that the mechanisms identified, the strains associated with each mechanism, and the proposed sequence of microstructural events are plausible.

DISCUSSION

Deformation in a foreland belt such as the central Appalachians begins with layer-parallel shortening preceding or coeval with propagation of thrusts (Geiser, 1988). This is followed by folding, either as a consequence of fault geometry (Suppe, 1983) or buckling. Integrating the results of the strain analysis with the sequence of mechanisms from microstructure cross-cutting relations suggests a plausible strain history consistent with the known events in this foreland belt. Age relations of microstructures indicate that pressure solution was the first mechanism. Shortening was normal to bedding (Fig. 6) which is consistent with chemical compaction during diagenesis. Compaction alone would not produce the observed preferred orientation of X- and Y-axes (Fig. 6), indicating that additional pressure solution occurred during a later event or that compaction was more complicated than uniaxial shortening. Couzens et al. (1993) describe a model whereby compaction can yield an asymmetric strain geometry in the plane of bedding as a result of tectonic activity in the basin during diagenesis. The next mechanism is dislocation creep which is inferred to have operated during layer-parallel shortening. This is supported by
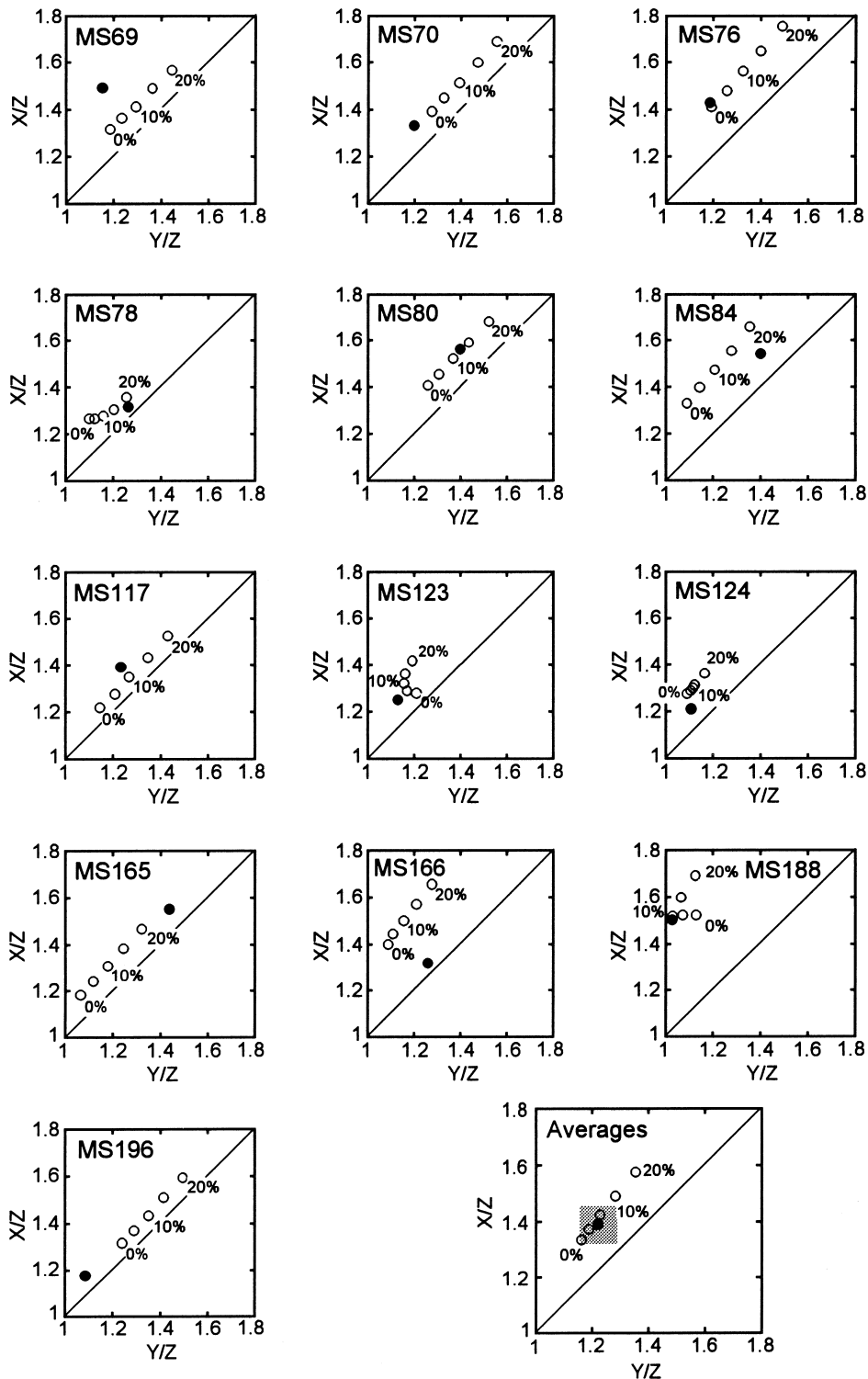
Fig. 8. X/Z vs Y/Z plots of factorized strains. Open circles represent different amounts of mechanical compaction (0–20%) used in the strain factorizations. Solid circle is measured finite strain. Last plot is average of 13 samples; shaded box is ±1 standard deviation about mean.

the dislocation creep strain geometry (Fig. 6) where shortening is parallel to bedding dip. Differential stresses are likely to have been at their highest during layer-parallel shortening (Dieterich and Carter, 1969) which is consistent with the location of the dislocation creep field relative to other mechanisms on deformation mechanism maps (Ashby and Verrall, 1977).

Additional pressure solution that is responsible for the preferred X- and Y-axis orientations of the pressure solution strain (Fig. 6) may have occurred at this time. The youngest mechanism is microfracturing. No consistent age relations between the three orthogonal sets of microfractures was found. It is also not possible to relate the microfractures to any regional deformational

event other than they must post-date layer-parallel shortening as microfractures cut deformation lamellae and bands (Fig. 3a & b). The only remaining regional event is folding; therefore, microfracturing is believed to be related to folding. In any case, bedding exerted a strong control on local stress orientations as shown by the relationship between microfracture strains and bedding (Fig. 6).

A similar strain history was described by Couzens *et al.* (1993) who recognized compaction followed by layer-parallel shortening, followed by folding. Of the three events recognized in their study, compaction was most important in its contribution to the finite strain.

CONCLUSIONS

Grain-scale deformation in the Massanutten Sandstone was accomplished by three deformation mechanisms: pressure solution, dislocation creep, and microfracturing. Of these, pressure solution was the most important in its overall contribution to the finite strain. Cross-cutting relations between associated microstructures indicate that these mechanisms operated sequentially, with each being associated with a regional event. Pressure solution occurred during compaction, prior to regional deformation. Dislocation creep occurred in response to high differential stresses that characterize layer-parallel shortening prior to folding. Microfracturing appears to be related to folding.

REFERENCES

Ashby, M. F. and Verrall, R. A. (1977) Micromechanics of flow and fracture, and their relevance to rheology of the upper mantle. *Philosophical Transactions of the Royal Society of London* **288A**, 58–95.

Carter, N. L., Christie, J. M. and Griggs, D. T. (1964) Experimental deformation and recrystallization of quartz. *Journal of Geology* **72**, 687–733.

Carter, N. L. (1968) Flow of rock-forming crystals and aggregates. In *Rock Mechanics Seminar*, ed. R. E. Riecker, pp. 509–594. U.S. Air Force Cambridge Research Laboratories, Clearing House for Federal Science and Technology Information AD 669 376, **2**.

Christie, J. M., Griggs, D. T. and Carter, N. L. (1964) Experimental evidence of basal slip in quartz. *Journal of Geology* **72**, 734–756.

Couzens, B. A., Dunne, W. M., Onasch, C. M. and Glass, R. (1993) Strain variations and three-dimensional strain factorization at the transition from the southern to the central Appalachians. *Journal of Structural Geology* **15**, 451–464.

Dieterich, J. H. and Carter, N. L. (1969) Stress history of folding. *American Journal of Science* **267**, 124–154.

Dunne, W. M., Onasch, C. M. and Williams, R. T. (1990) The problem of strain-marker centers and the Fry method. *Journal of Structural Geology* **12**, 933–938.

Epstein, A. G., Epstein, J. B. and Harris, L. D. (1977) *Conodont color alteration—an index to organic metamorphism.* U.S. Geological Survey, Professional Paper, **995**.

Erslev, E. A. (1988) Normalized center-to-center strain analysis of packed aggregates. *Journal of Structural Geology* **10**, 201–209.

Evans, M. (1989) The structural geometry and evolution of foreland thrust systems, northern Virginia. *Geological Society of America Bulletin* **101**, 339–354.

Geiser, P. A. (1988) Mechanisms of thrust propagation: some examples and implications for the analysis of overthrust terranes. *Journal of Structural Geology* **10**, 829–845.

Harris, A. G. (1970) Conodont color alteration, an organo-mineral metamorphic index, and its application to Appalachian Basin geology. In *Aspects of Diagenesis*, eds P. A. Scholle and P. R. Schluger, pp. 3–16. Special Publication of the Society of Economic Paleontologists and Mineralogists, **26**.

Harrison, M. A. (1997) Quantitative assessment of strain and deformation mechanisms in a folded quartz arenite. Unpublished M.Sc. thesis. Bowling Green State University, Ohio.

Hirth, G. and Tullis, J. (1992) Dislocation creep regimes in quartz aggregates. *Journal of Structural Geology* **14**, 145–159.

Houseknecht, D. W. (1988) Intergranular pressure solution in four quartzose sandstones. *Journal of Sedimentary Petrology* **58**, 228–246.

Lloyd, G. E. and Knipe, R. J. (1992) Deformation mechanism accommodating faulting of quartzite under upper crustal conditions. *Journal of Structural Geology* **14**, 127–143.

Manus, R. W. and Coogan, A. H. (1974) Bulk volume reduction and pressure solution derived cement. *Journal of Sedimentary Petrology* **44**, 466–471.

Mitra, S. (1976) A quantitative study of deformation mechanisms and finite strain in quartzites. *Contributions in Mineralogy and Petrology* **59**, 203–206.

Onasch, C. M. (1984) Petrofabric test of viscous buckling theory. *Tectonophysics* **106**, 141–153.

Onasch, C. M. (1990) Role of microfractures in the deformation of a quartz arenite in the central Appalachian foreland. *Journal of Structural Geology* **12**, 883–894.

Onasch, C. M. (1993) Determination of pressure solution shortening in sandstones. *Tectonophysics* **227**, 1–15.

Onasch, C. M. (1994) Assessing brittle volume-gain and pressure solution volume loss processes in quartz arenite. *Journal of Structural Geology* **16**, 519–530.

Onasch, C. M. and Dunne, W. M. (1993) Variation in quartz arenite deformation mechanisms between a roof sequence and duplexes. *Journal of Structural Geology* **15**, 465–476.

Owens, W. H. (1984) The calculation of a best-fit ellipsoid from elliptical sections on arbitrarily oriented planes. *Journal of Structural Geology* **6**, 571–577.

Suppe, J. (1983) Geometry and kinematics of fault-bend folding. *American Journal of Science* **283**, 684–721.

Thorbjornsen, K. L. and Dunne, W. M. (1997) Origin of a thrust-related fold: geometric vs kinematic tests. *Journal of Structural Geology* **19**, 303–320.

Tullis, J., Christie, J. M. and Griggs, D. T. (1973) Microstructures and preferred orientation of experimentally deformed quartzites. *Geological Society of America Bulletin* **84**, 297–314.

Wu, S. and Groshong, R. H., Jr. (1991) Strain analysis using quartz deformation bands. *Tectonophysics* **190**, 269–282.